

Searching for extreme mass ratio inspirals in LISA: from identification to parameter estimation

Stefan H. Strub,^{1,*} Lorenzo Speri,² and Domenico Giardini¹

¹*Institute of Geophysics, ETH Zurich
Sonneggstrasse 5, 8092 Zurich, Switzerland*

²*European Space Agency (ESA), European Space Research and Technology
Centre (ESTEC), Keplerlaan 1, 2201 AZ Noordwijk, the Netherlands*

The Laser Interferometer Space Antenna (LISA) is a planned space-based observatory designed to detect gravitational waves (GWs) within the millihertz frequency range. LISA is anticipated to observe the inspiral of compact objects into black holes at the centers of galaxies, so called extreme-mass-ratio inspirals (EMRIs). However, the extraction of these long-lived complex signals is challenging due to the large size and multimodality of the search space. In this study, we introduce a new search strategy that allows us to find EMRI signals in noisy data from wide priors all the way to performing parameter estimation. This work is an important step in understanding how to extract EMRIs from future LISA data.

Keywords: Gravitational Waves, LISA, Extreme-Mass-Ratio Inspirals, EMRI, LISA Data Challenge, Global Fit

I. INTRODUCTION

Extreme Mass Ratio Inspirals (EMRIs) are one of the key gravitational wave sources that the Laser Interferometer Space Antenna (LISA) is expected to detect [1, 2]. These signals originate from the inspiral of a stellar-origin compact object into a massive black hole (SMBH) typically residing at the center of a galaxy. EMRI systems are characterized by extremely small mass ratios $\mu/M \sim 10^{-4} - 10^{-6}$, where $\mu \sim 1 - 100 M_\odot$ is the mass of the orbiting secondary and $M \sim 10^5 - 10^7 M_\odot$ is the mass of the primary massive black hole. The formation details depend on the precise formation mechanism [3–5], but it is anticipated that most EMRIs will have non-negligible eccentricities at the plunge [1]. Eccentric orbits and small mass ratios lead to gravitational wave signals characterized by a rich harmonic content and tens of thousands of cycles in band. This makes EMRIs unique sources for extracting information about the nature of gravity [6–8] and the surroundings of SMBHs [9–11].

There are several challenges associated with realizing this rich scientific potential. In this work, we focus on the challenge of searching and identifying EMRIs. Unlike ground-based gravitational wave detectors, which can densely sample the parameter space using precomputed waveform banks, fully coherent template bank methods become impractical for EMRIs [5]. The posterior distribution characterizing EMRI signals occupies only a tiny fraction of this space, making it like searching for a needle in a cosmic haystack. As a result, conventional grid-based approaches are infeasible, leading to the adoption of semi-coherent searches and stochastic template placing.

Even with these techniques, identifying EMRI signals remains a complex task. The challenge arises from the

presence of numerous local maxima within the search landscape. These local maxima are due to non-local parameter degeneracies in the signal space [12]. In simpler terms, many combinations of parameters can produce waveforms that closely match the data, creating these local peaks in the optimization landscape. However, these local maxima are different from the true global maxima, which are located at entirely different parameter configurations and are often separated by vast distances in the parameter space. Distinguishing true EMRI signals from these local peaks is a complex puzzle.

The Mock LISA Data Challenges have demonstrated the difficulties associated with the detection of EMRI signals [13]. Previous works have adopted several strategies to address these two problems. Stochastic searches from [14, 15] got stuck on local maxima and tried to use such local maxima as information to move to the global maximum. An alternative approach was proposed in [16], where the use of a veto likelihood would remove the local maxima and allow only the global maxima to remain. Other approaches used phenomenological waveforms, where the initial stage is to identify harmonics and then search for possible EMRI parameters [17]. Ref. [18] introduced a sparse dictionary learning algorithm to reconstruct year-long EMRI waveforms. Ref. [19] developed a convolutional neural network for signal-to-noise ratios between 50 and 100, facilitating rapid detection and parameter estimation of EMRIs. Ref. [20] demonstrated the applicability of a convolutional neural network in the detection of EMRI signals. Ref. [21] combined template searches similar to [14, 15] with phenomenological waveform searchers [17]. However, they manage to constrain the parameters to the region where most of the secondaries lie around the primary peak.

In this work, we make a step forward with respect to [21] by reaching the primary peak and performing parameter estimation, simulating a full search and parameter estimation pipeline for a single EMRI in stationary

* stefan.strub@eaps.ethz.ch

Gaussian noise. We introduce a novel search statistic and employ it to achieve an accurate identification of EMRI signals, leading to the successful extraction of such signals. We define a successful signal extraction as a case where the difference between the recovered signal and the original GW signal in the data is significantly smaller in magnitude than the GW signal itself. This ensures that, after subtracting the recovered signal from the data, the residual can be effectively utilized to search for other GW signals. Furthermore, we performed parameter estimation using the parameters of the recovered signal, demonstrating the efficacy of our method in extracting EMRI signals and obtaining their posterior distributions.

II. METHODS

A. LISA Data Analysis

The basic observables of LISA are the Time Delay Interferometry variables. These variables are constructed from six Doppler measurements in order to suppress laser frequency noise. In this work, we adopt the pseudo-orthogonal combinations A and E and exclude the channel T , which is suppressed below the transfer frequency $f_* = 1/(2\pi L) \approx 19.1$ mHz [22–24].

We treat channels A and E as outputs from independent instruments. We assume that each channel is a time series, denoted as $d(t)$, and consists of the superposition of multiple gravitational wave (GW) signals and instrumental noise, $n(t)$. Here, we consider the case of a single EMRI source $s(t, \theta)$ present in the data:

$$d(t) = s(t, \theta) + n(t). \quad (1)$$

For simplicity, we omit explicit time dependence in subsequent expressions, considering d , $s(\theta)$, and n as time series.

To simulate the signal component $s(\theta)$ of the LISA data, we use the FastEMRIWaveform package **few** [25–33] to obtain the gravitational wave signal in the solar system barycenter and the fast lisa response package [34] to include the LISA response and produce the TDI outputs, and therefore obtain the signal $s(\theta)$. We consider EMRI waveforms of non-spinning black holes, which are described by 11 parameters:

$$\theta = \{M, \mu, p_0, e_0, D_L, \theta_S, \phi_S, \Phi_{\varphi 0}, \Phi_{r0}, \theta_K, \phi_K\}. \quad (2)$$

Here, M represents the mass of the central massive black hole, while μ denotes the mass of the secondary object. Orbital elements are characterized by the semi-latus rectum p_0 and eccentricity e_0 . The source's sky location in the Solar System barycenter frame is given by the angles θ_S and ϕ_S , while the orientation of the binary's orbital angular momentum is specified by θ_K and ϕ_K . The luminosity distance is denoted by D_L . The initial orbital phases are $\Phi_{\varphi 0}$ and Φ_{r0} .

TABLE I: Parameters of the injected EMRI.

Parameter	Injected Value
M (M_\odot)	10^6
μ (M_\odot)	10
e_0	0.2
t_p (yr)	0.44
p_0	8.5072
D_L (Gpc)	0.85
θ_S	$3\pi/4$
ϕ_S	$3\pi/4$
$\Phi_{\varphi 0}$	1
Φ_{r0}	3
θ_K	$3\pi/4$
ϕ_K	$3\pi/4$
ρ_{optimal}	56

The simulated LISA data consist of an EMRI signal with the parameter values listed in Table I. The intrinsic parameters of the EMRI are consistent with those used in [35]. The time to plunge t_p is set to 0.44 years.

The injection noise n is modeled using **LISAtools** [36], with the *FittedHyperbolicTangentGalacticForeground* model used to estimate the galactic noise over a six-month period. Figure 1 presents the spectrogram of the EMRI signal injected into the TDI A channel alongside the noisy data for the input and the recovered EMRI signal. Additionally, Figure 4 presents the noisy data, the EMRI signal, and the corresponding power spectral density (PSD) curve in the frequency domain, illustrating the reduction in noise around 4 mHz.

B. Likelihood and signal-to-noise ratio

The likelihood function $p(d|\theta)$ quantifies the probability of observing data d given the source parameters θ . Under the assumption of stationary Gaussian noise, the likelihood for one channel can be obtained with

$$\log p(d|\theta) \propto -\frac{1}{2} \langle d - s(\theta), d - s(\theta) \rangle, \quad (3)$$

where the inner product of two signals $x(t)$ and $y(t)$ in the frequency domain is defined as:

$$\langle x, y \rangle = 4\mathcal{R} \int_0^\infty \frac{\tilde{x}(f)\tilde{y}^*(f)}{S_n(f)} df, \quad (4)$$

where $\tilde{x}(f)$ is the Fourier transform of $x(t)$, and $S_n(f)$ is the one-sided power spectral density of the noise [36].

A proxy to find the best-fit parameters θ' given a dataset is to maximize the matched signal-to-noise ratio (SNR), given by:

$$\rho = \frac{\langle d, s(\theta') \rangle}{\sqrt{\langle s(\theta'), s(\theta') \rangle}}, \quad (5)$$

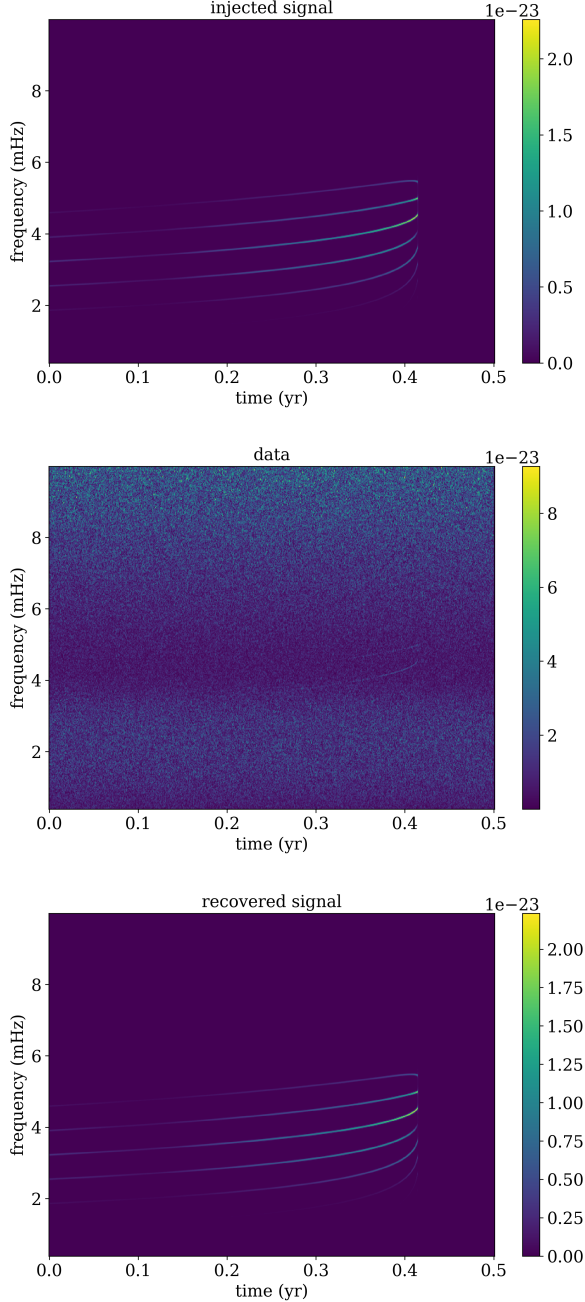


FIG. 1: Spectrogram of the TDI A channel of the noisy data, the injected and recovered signal.

which is independent of the luminosity distance D_L . The optimal estimate for D_L maximizing the likelihood is:

$$D_L = \frac{\langle s(\theta'), s(\theta') \rangle}{\langle d, s(\theta') \rangle}, \quad (6)$$

where $\theta' = \theta \setminus \{D_L\}$. The optimal SNR is defined as:

$$\rho_{\text{optimal}} := \sqrt{\langle s(\theta), s(\theta) \rangle}, \quad (7)$$

which differs from the detected SNR due to noise fluctuations.

C. Matching spectrograms

The difficulty in extracting extreme mass-ratio inspirals arises from the nonlocal parameter degeneracies and the fact that both the primary and secondary modes for standard search statistics are extremely small compared to the search volume. The narrow primary peak of the SNR statistic makes it particularly difficult to find the primary. Our goal is to increase the size of the primary peak by changing the search statistic.

Instead of using the fully coherent search statistic ρ of Eq. 5, we propose to maximize the following new search statistic

$$\mathcal{S}^\lambda := \frac{\langle d, s(\theta) \rangle_{\text{tf}, \lambda}}{\sqrt{\langle s(\theta), s(\theta) \rangle_{\text{tf}, \lambda}}}, \quad (8)$$

with the time-frequency inner product defined as

$$\langle x, y \rangle_{\text{tf}, \lambda} := \left[\sum_{\tau=0}^{N-1} 4\mathcal{R} \int_0^\infty \left(\frac{|\tilde{x}_\tau(f)| |\tilde{y}_\tau(f)|}{S_n(f)} \right)^\lambda df \right]^{1/\lambda}, \quad (9)$$

with $\tilde{x}_\tau(f)$ being the short Fourier transform of the time series $x(t)$ for the first time window τ .

We adopt the short-time Fourier transform representation of the data in order to find the best parameters that match the power in each time-frequency “pixel”. Therefore, the function \mathcal{S} has the advantage of disregarding the phase coherence between pixels but still imposes the frequency evolution coherence. This provides a wider primary mode in the search landscape for parameters $\{M, \mu, p_0, e_0\}$ as shown in Fig. 2 for the source of Table I.

We observe that the primary peak for the SNR function, ρ , is narrow compared to the search space. Instead, for \mathcal{S} , the primary mode is significantly wider, increasing the chance of convergence for a stochastic search.

The function \mathcal{S} can be used to optimize parameters $\{M, \mu, p_0, e_0\}$, allowing us to refine the prior distribution before conducting a follow-up search optimizing the SNR ρ .

The exponent λ acts as a generalized mean [37, 38] and can be adjusted to enhance the efficiency of the parameter optimization algorithm. As illustrated in Fig. 3, when drawing 1000 random samples from the prior, $\mathcal{S}^{\lambda=1}$ and $\mathcal{S}^{\lambda=2}$ sometimes produce higher match statistics for incorrect parameter sets than for the injected values. This suggests that these values of λ are unsuitable, as they allow secondary modes or noise realizations to dominate over the true parameters. Increasing λ mitigates this effect by suppressing noise-induced matches, effectively raising the threshold for acceptable match accuracy. As an additional effect, for larger λ , the primary mode becomes narrower, making it more challenging to locate

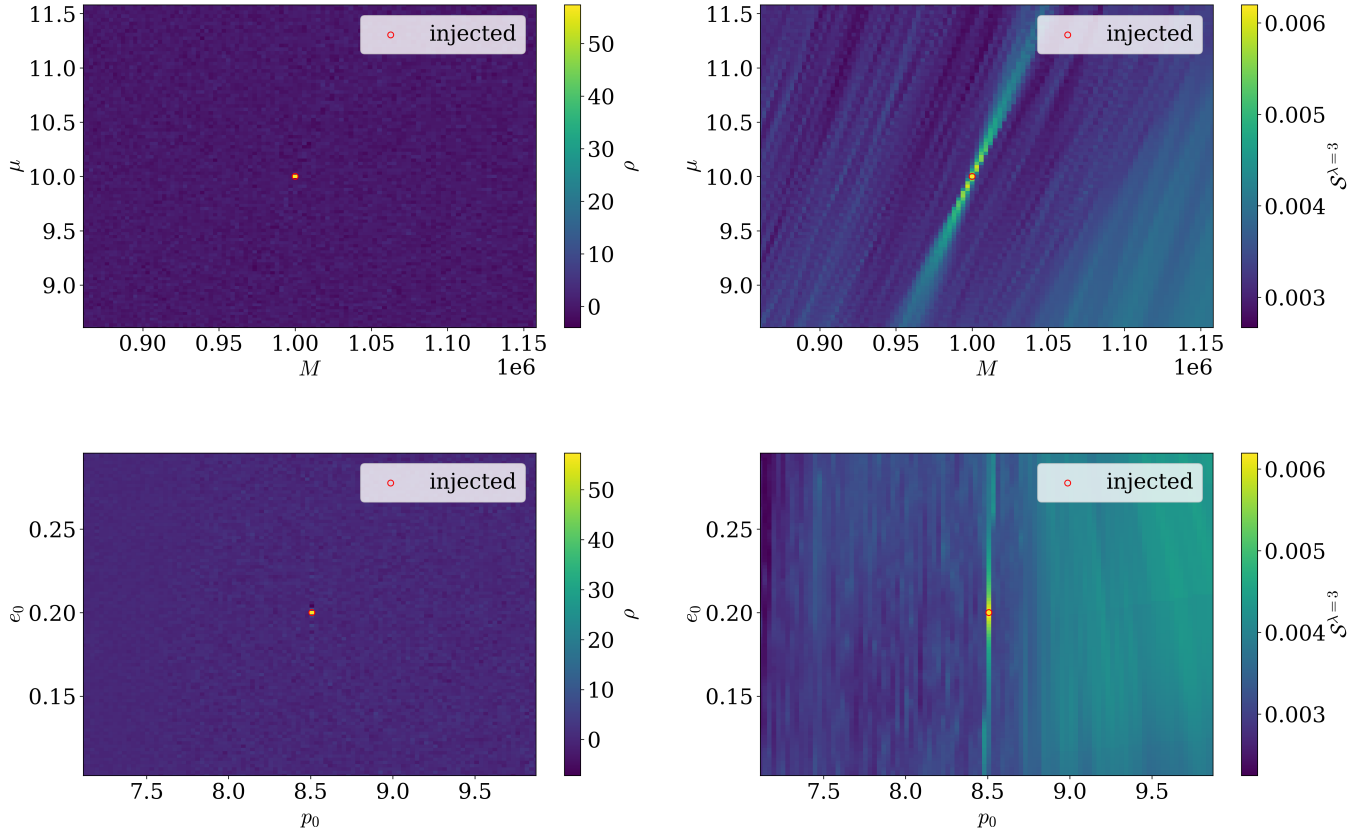


FIG. 2: Search functions computed varying only two parameters at a time. The left panels show the SNR function, while the right panels display the power spectrum matching. The top panels vary the masses, while the middle and bottom panels vary the eccentricity and semi-latus rectum.

during optimization. As seen in the bottom left panel of Fig. 2, $\mathcal{S}^{\lambda=1}$ exhibits secondary modes that exceed the match statistic of the injected parameters. Meanwhile, the bottom right panel shows that $\mathcal{S}^{\lambda=4}$ results in a narrower primary mode compared to $\mathcal{S}^{\lambda=3}$.

To balance these effects, we set $\lambda = 3$ for the remainder of this study, as it is the smallest value for which secondary modes do not exceed the match statistic of the injected parameters.

A limitation of optimizing \mathcal{S} is that it inherently reduces sensitivity to certain signals. Specifically, it restricts detection to those with sufficiently high SNR, potentially missing weaker or more diffuse signals. An extensive investigation of this search statistic through the entire EMRI parameter space is left for future work.

D. Noise Estimation

The noise estimation process is performed across the full frequency band, following a modified approach based on [39], originally introduced in [40]. In the following, we provide a concise overview of the pipeline and the

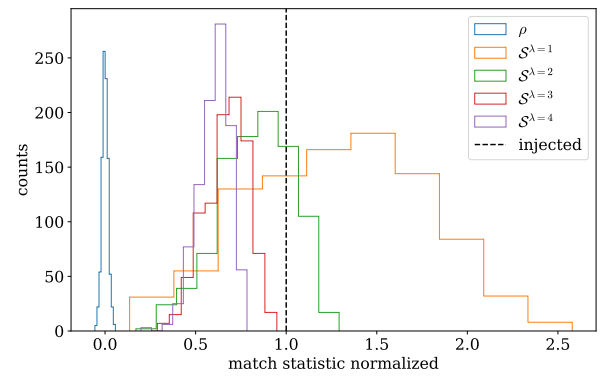


FIG. 3: Histogram of different detection statistics for 1000 randomly drawn samples from the prior distribution. Each statistic is normalized with respect to its value at injection.

modifications applied.

The noise estimation process begins with Welch's method, where the initial power spectral density (PSD)

is computed. To mitigate outlier peaks, we employ a 30-bin moving window, replacing extreme values with the median while iteratively shifting by 15 bins. To further smooth the estimate, a Savitzky-Golay filter is applied. The final residual noise curve is then obtained via spline interpolation.

Unlike the approach in [39], we modify Welch's method by replacing the fixed window size of 15,000 samples with a dynamic size of $75,000/dt$, where dt is the data cadence. This allows for varying signal sampling rates.

Additionally, to further refine the estimated noise, we apply a second Savitzky-Golay filter after the first. This secondary filter has a polynomial degree of 1 and a window length of 5, improving the smoothness of the final noise curve.

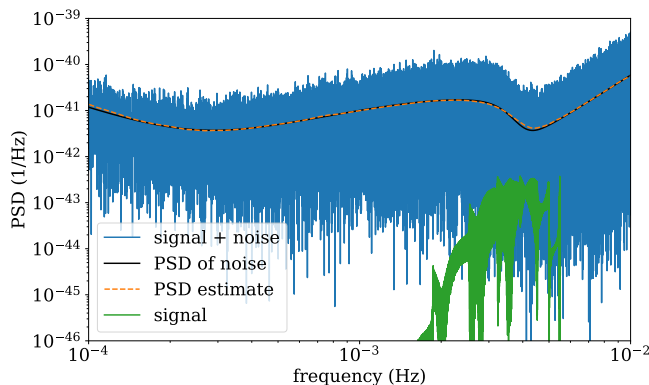


FIG. 4: Noise estimation for the data shown in Fig. 1. The data (noise and signal realizations) are shown in blue. The assumed and recovered PSD are shown in black and dashed orange, respectively, for the TDI A channel. In green we show the signal of the EMRI.

Fig. 4 presents the noise estimate for the LDC2a data set. The estimated noise generally aligns with the PSD used to generate the noise realization with a relative error of 3% within the frequency range of $[0.4 \text{ mHz}, 10 \text{ mHz}]$.

E. The Pipeline

To search for a signal, we need to define some priors. Here, we adopt the one shown in Table II. Most are linearly uniform, with exceptions: θ_S and θ_K follow a cosine-uniform distribution, while M and μ are log-uniform. Furthermore, the prior boundaries for the initial eccentricity e_0 are limited to the validity region of the current waveform simulator.

Initially, the noise power spectral density $S_n(f)$ is estimated, which is a key component for calculating the scalar products in Eqs. 4 and 9. For the analysis presented here, we first optimize $\mathcal{S}_{\text{noresponse}}$, where we compute \mathcal{S} directly using the simulated GW signal, disregarding the LISA response. This approach restricts the search

for parameters to the intrinsic variables $\{M, \mu, p_0, e_0\}$, bypassing the need for sky location matching.

Sampling over p_0 within the full prior range can lead to signals that fall outside the valid domain of **few**. To address this, the first iteration of the search restricts the prior on the time to plunge, t_p , to a two-week window. The value of p_0 is then determined numerically from the set $\{t_p, M, \mu, e_0\}$ using Brent's method and by evolving the inspiral and identifying the value of p_0 that produces the specified t_p . This function for calculating p_0 is implemented in **few**.

The initial search may become trapped in local maxima, far from the injected values. To mitigate this, we repeat the initial search optimization $\mathcal{S}_{\text{noresponse}}$ three times and choose the set of parameters with the highest value $\mathcal{S}_{\text{noresponse}}$. After initial optimization, we obtain estimates for the parameters $\{M, \mu, p_0, e_0\}$ that are close to the injected values. This allows us to narrow the prior and center it around the estimated parameters. From now on, we are sampling p_0 instead of t_p .

The next step involves optimizing \mathcal{S} , with the parameter set found previously serving as an initial guess. After refining the parameter space around the recovered values $\{M, \mu, p_0, e_0\}$, we perform a final optimization by maximizing the standard SNR ρ as defined in Eq. 5. The optimization of $\mathcal{S}_{\text{noresponse}}$ and \mathcal{S} is relatively quick, which we limit to only 150 and 200 iterations, respectively, while optimizing ρ , we limit to 4000 iterations.

Once the optimization process is completed, the luminosity distance D_L is determined according to Eq. 6. Finally, the parameter boundaries are further refined and an MCMC algorithm is used to obtain the posterior distribution. A detailed summary of the pipeline is presented in Algorithm 1 as pseudocode.

TABLE II: The prior distribution Θ_{prior} for EMRIs.

Parameter	Boundary
$\log M \text{ (M}_\odot\text{)}$	$[\log 5 \cdot 10^5, \log 10^7]$
$\mu \text{ (M}_\odot\text{)}$	$[\log 5, \log 100]$
p_0	set by $\{t_p, M, \mu, e_0\}$
t_p	$[0.42, 0.46]$
e_0	$[0.01, 0.5]$
$D_L \text{ (Gpc)}$	$[0.01, 100]$
$\cos \theta_S$	$[-1, 1]$
ϕ_S	$[0, 2\pi]$
$\Phi_{\varphi 0}$	$[0, 2\pi]$
Φ_{r0}	$[0, 2\pi]$
$\cos \theta_K$	$[-1, 1]$
ϕ_K	$[0, 2\pi]$

After successfully detecting a signal, we perform an MCMC analysis. For this purpose, we use the **Eryn** MCMC sampler [41–43], configured with four temperatures, 32 walkers, 3000 samples, and 1000 burn-in samples. The resulting chain is used to compute the posterior distribution.

Algorithm 1: The EMRI search algorithm to analyze a data segment d with function f to optimize. The argmax is found using the differential evolution algorithm.

Function *EMRI_search*(d)

Estimate the noise $S_n(f)$

θ_{init} start guess randomly drawn from prior

Set boundaries to prior

$\theta_{\text{max}} \leftarrow \text{argmax}_{\theta} \mathcal{S}_{\text{noresponse}}^{\lambda=3}(\theta, d)$ with start θ_{init} and choosing p_0 such that t_p within a given two week window

Set boundaries of $\{M, \mu, p_0, e_0\}$ to $\{M(1 \pm 1\%), \mu(1 \pm 10\%), p_0 \pm 0.1, e_0 \pm 0.05\}$ of the found parameters

$\theta_{\text{max}} \leftarrow \text{argmax}_{\theta} \mathcal{S}^{\lambda=3}(\theta, d)$ with start θ_{max}

Set boundaries of $\{M, \mu, p_0, e_0\}$ to $\{M(1 \pm 0.5\%)M, \mu(1 \pm 5\%), p_0 \pm 0.05, e_0 \pm 0.025\}$ of the found parameters

$\theta_{\text{MLE}} \leftarrow \text{argmax}_{\theta} \rho(\theta, d)$ with start θ_{max}

Compute D_L according to Eq. (6) with θ_{MLE}

Set prior boundaries of $\{M, \mu, p_0, e_0, D_L\}$ to $\{M(1 \pm 0.01\%), \mu(1 \pm 0.1\%), p_0 \pm 0.001, e_0 \pm 0.001, D_L(1 \pm 10\%)\}$ of the found parameters

Use the found θ_{MLE} as the initial proposal for an MCMC algorithm within the reduced boundaries to obtain the posterior

return θ_{MLE} and MCMC chain

III. RESULTS

For this analysis, we adopted a sampling interval of $dt = 50$ s, under the assumption that no significant signal components exceed the Nyquist frequency, $f_{\text{Nyquist}} = 1/(2dt) = 10$ mHz. Time-frequency analysis was performed using the `stft` function from the SciPy library [44]. We used a Hann window with an overlap of 50% and set the segment length to $50000/dt$, optimizing the resolution in both the time and frequency domains.

The boundary of the time to plunge t_p is set to be a two week interval. Either the pipeline for obtaining θ_{MLE} is repeatedly performed with a moving window for the t_p prior, or a previous detection algorithm determined an EMRI signal within a given time interval for t_p . If no previous detection has been made, the algorithm can still be applied, and if the identified signal has an SNR above a certain threshold the signal is determined as a detection. In this article, we are using differential evolution (DE) [45] to maximize $\mathcal{S}_{\text{noresponse}}$, \mathcal{S} , and ρ .

A. Extraction of an SNR 56 Signal

To assess signal recovery, we applied our detection pipeline to the dataset illustrated in Fig. 1, using injection parameters corresponding to Table I. The iterative search for parameters, visualized in Fig. 6 and Fig. 7, enabled an iterative reduction in the prior distribution of key parameters $\{M, \mu, p_0, e_0\}$. This refinement helped identify the primary mode of the SNR function, ρ , and ultimately led to the convergence of the maximum likelihood estimate θ_{MLE} , with recovered parameters closely matching the injected values.

The recovered parameters are presented in Table III and visualized in the frequency domain in Fig. 5. The injected and recovered parameters are in close agreement, where the difference is one order of magnitude lower than

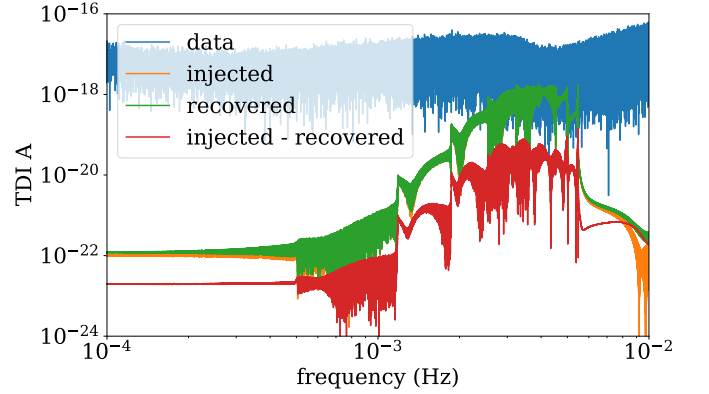


FIG. 5: The data, injected and recovered signal in the frequency domain. The signal parameters are listed in Table III.

the injected signal. Notably, the detected SNR of the recovered signal slightly surpasses that of the injected signal, which can be attributed to noise fluctuations. The condition $\rho(\theta_{\text{MLE}}) > \rho(\theta_{\text{injected}})$ further validates the success of the optimization procedure in refining the parameter search.

To finalize the results with a posterior distribution, we employed `Eryn` to generate an MCMC chain. The resulting corner plot in Fig. 8 excludes some parameters for better visualization. The complete corner plot with all parameters is added to Appendix A shown in Fig. 11. It is noticeable that the injected parameters are within the 68% probability region of the parameter estimation for all parameters except the phase Φ_{φ_0} .

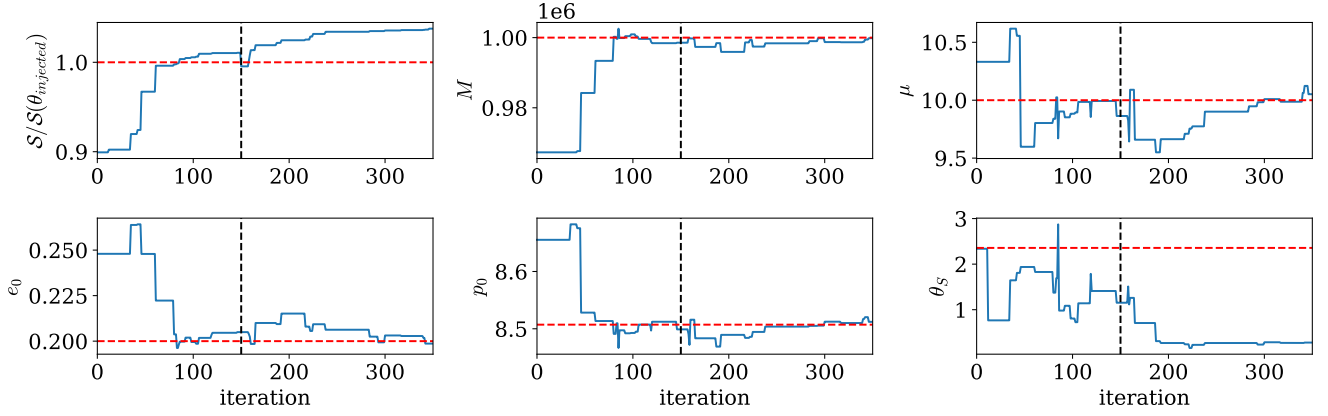


FIG. 6: The search chain of optimizing $\mathcal{S}_{\text{noresponse}}$ in the first 150 iteration and \mathcal{S} from iteration 151 to 350. The black vertical lines show the change in the optimization function. The dashed red lines show the injected values. The top left panel shows the optimization metric normalized by the value of the injection.

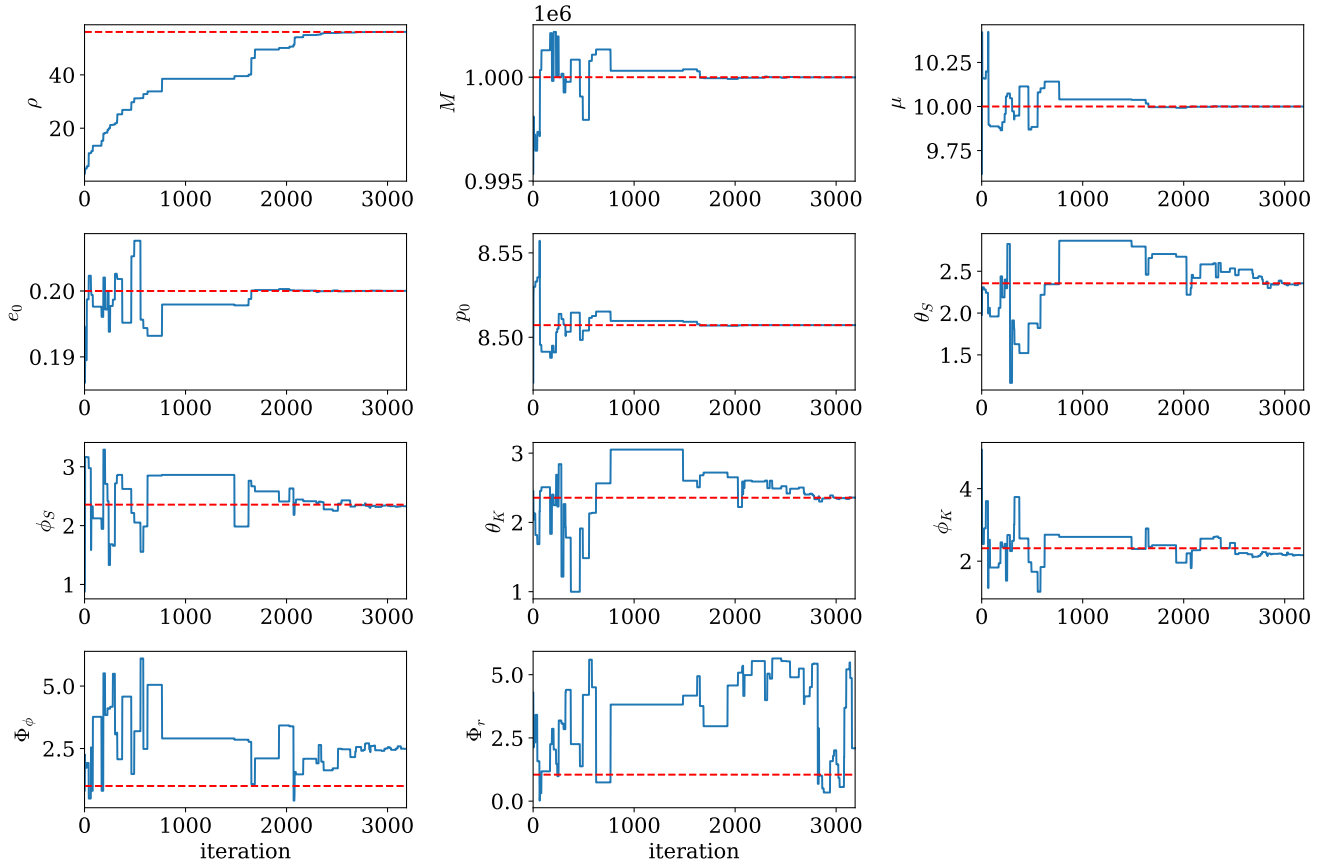


FIG. 7: The search chain of optimizing the SNR ρ . The dashed red lines show the injected values.

B. Increasing the mass

In a second example, we modify the EMRI by increasing the mass of the massive black hole and setting the distance to 0.2 Gpc. The differential evolution algorithm

optimizing ρ completes after 2,373 iterations, resulting in a reduced computational time. The injected and recovered parameters are summarized in Table IV. Figures 9 and 10 illustrate the search chains leading to the recovered values. We then calculate the posterior distribution

TABLE III: The injected and recovered parameters of the EMRI signal. The uncertainties are computed with the MCMC chain, which is shown as a corner plot in Fig. 8. Here we show the detected SNR ρ according to Eq. 5.

Parameter	Injected	Recovered
M (M_\odot)	10^6	999991 ± 20
μ (M_\odot)	10	9.9998 ± 0.0011
e_0	0.2	0.20003 ± 0.000075
p_0	8.5072	8.50719 ± 0.00006
D_L (Gpc)	0.85	0.855 ± 0.02
$\cos \theta_S$	-0.71	-0.71 ± 0.06
ϕ_S	2.36	2.33 ± 0.07
$\Phi_{\varphi 0}$	1	2.5 ± 0.7
Φ_{r0}	3	3.0 ± 0.3
$\cos \theta_K$	-0.71	-0.71 ± 0.09
ϕ_K	2.36	2.17 ± 0.09
ρ	56.09	56.12

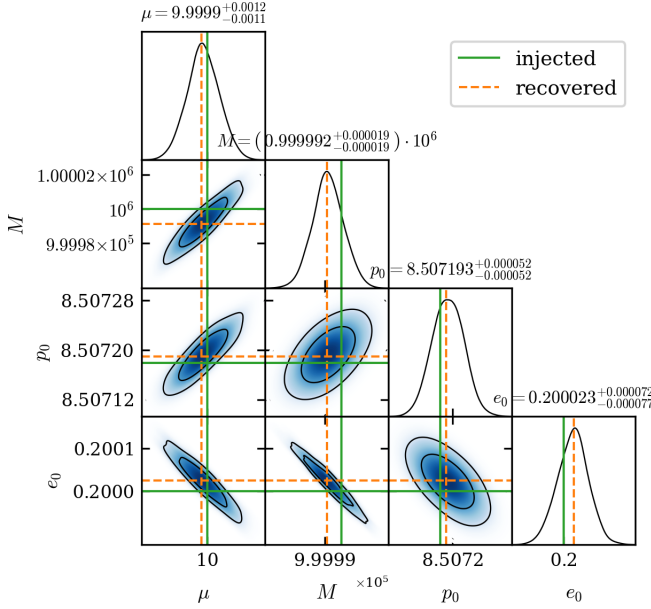


FIG. 8: Green solid lines denote the injected parameters, while orange dashed lines correspond to the recovered parameters, θ_{MLE} , presented in Table III. The blue contours illustrate the 68% and 95% confidence intervals for the parameter estimates. The posterior distribution is computed using θ_{MLE} as the initial condition for the MCMC sampling. The full posterior Figure 11 with all parameters can be found in the appendix A.

using an MCMC chain, with the corner plot shown in Fig. 12 in the Appendix A. Notably, the injected parameters fall within the 68% confidence interval for all parameters except for the phase $\Phi_{\varphi 0}$. The accuracy and precision of the recovered parameters are higher than those of the first signal, probably because of the higher SNR of the

injected signal.

TABLE IV: The injected and recovered parameters of the EMRI signal. The uncertainties are computed with the MCMC chain, which is shown as a corner plot in Fig. 8.

Parameter	Injected	Recovered
M (M_\odot)	1500000	1499998 ± 15
μ (M_\odot)	10	10.0003 ± 0.0009
e_0	0.2	0.2 ± 0.00005
p_0	7.8119	7.8119 ± 0.00003
D_L (Gpc)	0.2	0.201 ± 0.006
$\cos \theta_S$	-0.71	-0.71 ± 0.03
ϕ_S	2.36	2.34 ± 0.04
$\Phi_{\varphi 0}$	1	2.1 ± 0.9
Φ_{r0}	3	2.9 ± 0.2
$\cos \theta_K$	-0.71	-0.74 ± 0.05
ϕ_K	2.36	2.24 ± 0.12
ρ	81.62	81.66

C. Computational cost

The current setup requires 140 function evaluations per iteration for parameter optimization. Consequently, obtaining θ_{MLE} involves 510,000 function evaluations in 3,838 iterations. The time for the evaluation of each function is influenced by the efficiency of the waveform model, the LISA response computation, the statistic calculation of the match, and the computational hardware. With the implementation of `few` and the use of a mobile computer with a Quadro RTX 4000 mobile GPU, the computation of ρ and \mathcal{S} takes approximately 67 ms, while $\mathcal{S}_{\text{noresponse}}$ takes 34 ms. Thus, optimizing $\mathcal{S}_{\text{noresponse}}$ for 450 iterations, \mathcal{S} for 200 iterations, and ρ for 3188 iterations takes roughly 10.9 h on a laptop. When searching for the signal with the parameters of Table IV, the optimization of ρ concluded after 2,373 iterations, reducing the computational time to about 7.3 h.

The time required to generate the posterior distribution is determined primarily by the desired chain length. For a chain with 3000 samples, 32 walkers, four temperatures, and 1000 burn-in samples, the process takes approximately 8 h. Runtimes can be significantly reduced using high-performance computing resources.

IV. CONCLUSIONS

The first successful identification and inference of EMRI signals was achieved by optimizing a novel match statistic, which helped alleviate the complexities arising from nonlocal parameter degeneracies. Our pipeline can detect and estimate the parameters of the EMRI signals, even in the presence of instrument noise and the galactic foreground. This accomplishment represents a significant

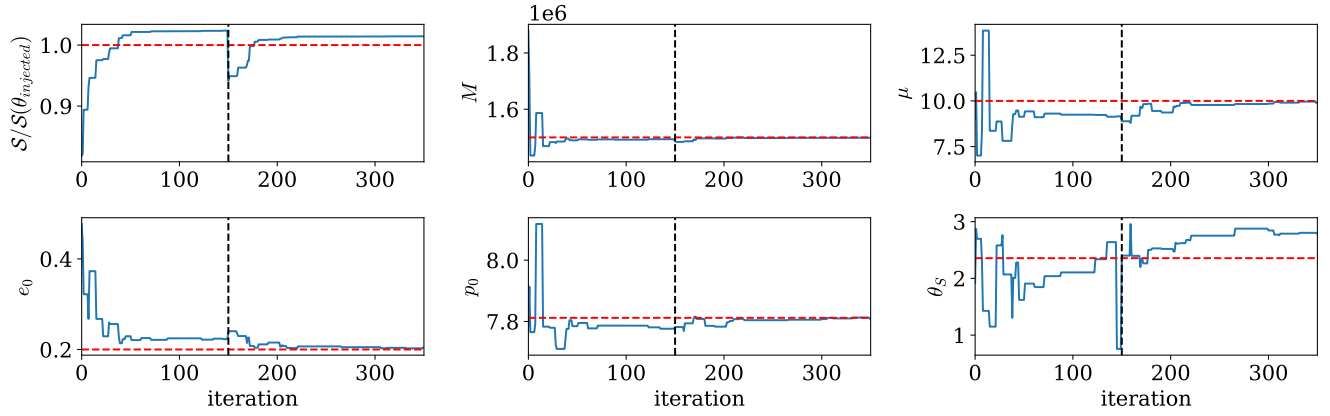


FIG. 9: Search for the increased mass signal. The resulting chain optimizes $\mathcal{S}_{\text{noresponse}}$ during the first 150 iterations, followed by optimization of \mathcal{S} from iteration 151 to 350. Black vertical lines indicate the transition between the two objective functions. Dashed red lines mark the injected parameter values. The top-left panel displays the optimization metric, normalized by its value at the injection.

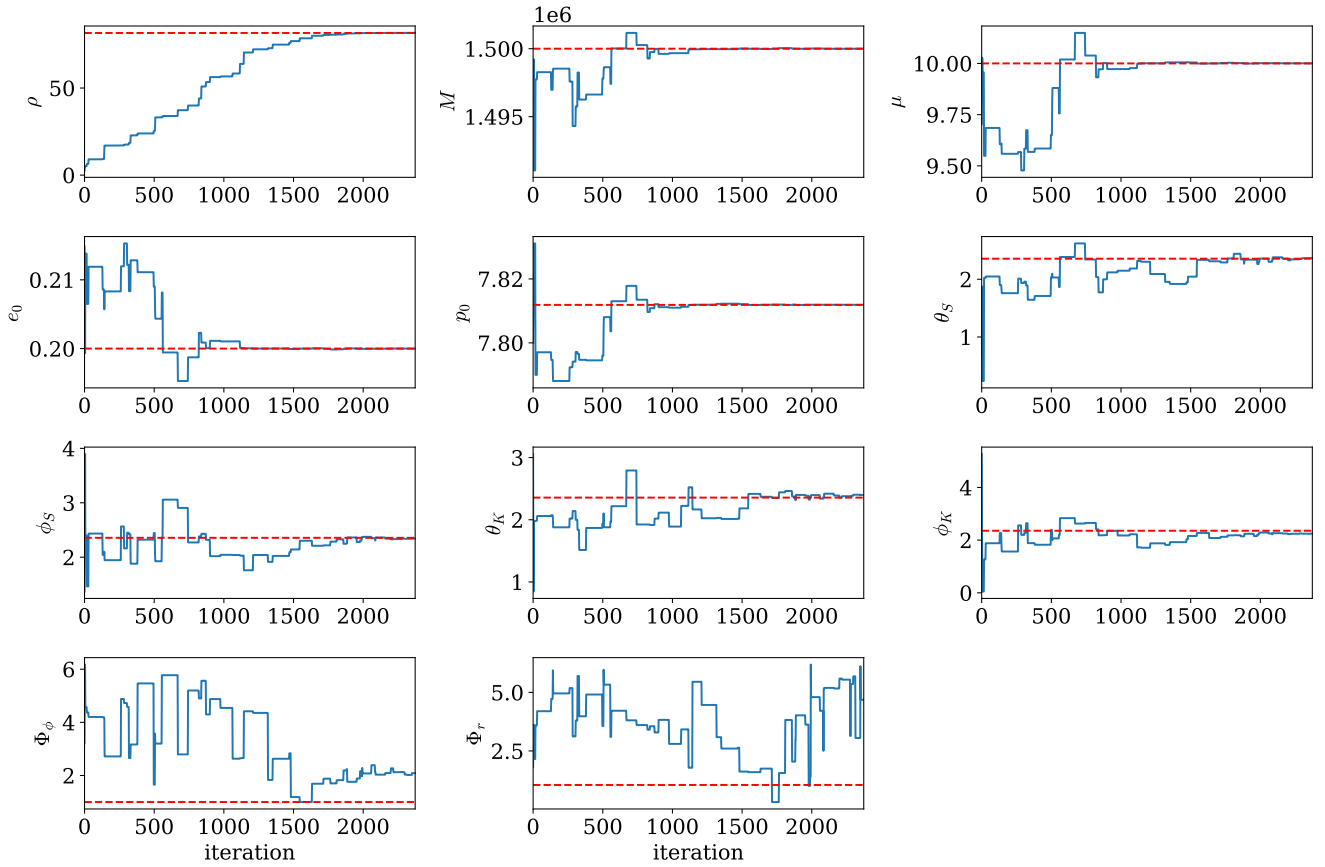


FIG. 10: Search for the increased mass signal, performed by optimizing the SNR ρ . The dashed red lines indicate the injected parameter values.

step forward in the preparation for the LISA mission and opens up exciting prospects for probing the universe's most extreme environments. Detecting and analyzing

EMRI signals will allow astrophysicists to test general relativity in strong gravitational fields, investigate the formation and evolution of supermassive black holes, and

possibly uncover physics beyond the standard model of cosmology. Moreover, accurately identifying signals plays a crucial role in minimizing their interference by subtracting them from the data, facilitating the identification of other sources in a global analysis pipeline. This pipeline paves the way for studying the interplay between different types of gravitational wave sources, including EMRIs.

A current limitation of the method is its reliance on relatively high-SNR signals that stand out within a noisy power spectrum. In this study, we successfully estimated parameters for a signal with an optimal SNR of $\rho_{\text{optimal}} = 56$. Future work will aim to improve the sensitivity to weaker signals by refining the match statistic and exploring the performance limits of minimum SNR and signal duration. Additionally, incorporating spinning black holes into the analysis will introduce new complexities that will need to be addressed in future work.

V. ACKNOWLEDGEMENTS

We are thankful for the GPU implementation of `few` and all previous work on ERMI signal simulation and

search, which enabled this work. This work was supported by GW-Learn, a project funded by a Sinergia grant from the Swiss National Science Foundation.

Appendix A: Posteriors

We present the full posterior distributions of the samples discussed in the results. Figure 11 shows the posterior distributions for all signal parameters corresponding to the injection values listed in Table I. Similarly, Figure 12 displays the posterior distributions for the signal parameters associated with the values in Table IV.

-
- [1] S. Babak, J. Gair, A. Sesana, E. Barausse, C. F. Sopuerta, C. P. L. Berry, E. Berti, P. Amaro-Seoane, A. Petiteau, and A. Klein, Science with the space-based interferometer LISA. V: Extreme mass-ratio inspirals, *Phys. Rev. D* **95**, 103012 (2017), [arXiv:1703.09722 \[gr-qc\]](#).
 - [2] M. Colpi, K. Danzmann, M. Hewitson, K. Holley-Bockelmann, P. Jetzer, G. Nelemans, A. Petiteau, D. Shoemaker, C. Sopuerta, R. Stebbins, *et al.*, LISA definition study report, arXiv preprint [arXiv:2402.07571](#) (2024).
 - [3] P. Amaro-Seoane, Relativistic dynamics and extreme mass ratio inspirals, *Living Rev. Rel.* **21**, 4 (2018), [arXiv:1205.5240 \[astro-ph.CO\]](#).
 - [4] C. P. L. Berry, S. A. Hughes, C. F. Sopuerta, A. J. K. Chua, A. Heffernan, K. Holley-Bockelmann, D. P. Mihaylov, M. C. Miller, and A. Sesana, The unique potential of extreme mass-ratio inspirals for gravitational-wave astronomy (2019), [arXiv:1903.03686 \[astro-ph.HE\]](#).
 - [5] J. R. Gair, L. Barack, T. Creighton, C. Cutler, S. L. Larson, E. S. Phinney, and M. Vallisneri, Event rate estimates for LISA extreme mass ratio capture sources, *Class. Quant. Grav.* **21**, S1595 (2004), [arXiv:gr-qc/0405137](#).
 - [6] L. Speri, S. Barsanti, A. Maselli, T. P. Sotiriou, N. Warburton, M. van de Meent, A. J. K. Chua, O. Burke, and J. Gair, Probing fundamental physics with Extreme Mass Ratio Inspirals: a full Bayesian inference for scalar charge (2024), [arXiv:2406.07607 \[gr-qc\]](#).
 - [7] L. Barack and C. Cutler, Using LISA EMRI sources to test off-Kerr deviations in the geometry of massive black holes, *Phys. Rev. D* **75**, 042003 (2007), [arXiv:gr-qc/0612029](#).
 - [8] C. F. Sopuerta and N. Yunes, Extreme and Intermediate-Mass Ratio Inspirals in Dynamical Chern-Simons Modified Gravity, *Phys. Rev. D* **80**, 064006 (2009), [arXiv:0904.4501 \[gr-qc\]](#).
 - [9] J. R. Gair, C. Tang, and M. Volonteri, LISA extreme-mass-ratio inspiral events as probes of the black hole mass function, *Phys. Rev. D* **81**, 104014 (2010), [arXiv:1004.1921 \[astro-ph.GA\]](#).
 - [10] L. Speri, A. Antonelli, L. Sberna, S. Babak, E. Barausse, J. R. Gair, and M. L. Katz, Probing Accretion Physics with Gravitational Waves, *Phys. Rev. X* **13**, 021035 (2023), [arXiv:2207.10086 \[gr-qc\]](#).
 - [11] P. S. Cole, G. Bertone, A. Coogan, D. Gaggero, T. Karydas, B. J. Kavanagh, T. F. M. Spieksma, and G. M. Tomaselli, Distinguishing environmental effects on binary black hole gravitational waveforms, *Nature Astron.* **7**, 943 (2023), [arXiv:2211.01362 \[gr-qc\]](#).
 - [12] A. J. K. Chua and C. J. Cutler, Nonlocal parameter degeneracy in the intrinsic space of gravitational-wave signals from extreme-mass-ratio inspirals, *Phys. Rev. D* **106**, 124046 (2022), [arXiv:2109.14254 \[gr-qc\]](#).
 - [13] S. Babak, J. G. Baker, M. J. Benacquista, N. J. Cornish, S. L. Larson, I. Mandel, S. T. McWilliams, A. Petiteau, E. K. Porter, E. L. Robinson, *et al.*, The mock lisa data challenges: from challenge 3 to challenge 4, *Classical and Quantum Gravity* **27**, 084009 (2010).
 - [14] S. Babak, J. R. Gair, and E. K. Porter, An Algorithm for detection of extreme mass ratio inspirals in LISA data, *Class. Quant. Grav.* **26**, 135004 (2009), [arXiv:0902.4133 \[gr-qc\]](#).
 - [15] N. J. Cornish, Detection Strategies for Extreme Mass Ratio Inspirals, *Class. Quant. Grav.* **28**, 094016 (2011), [arXiv:0804.3323 \[gr-qc\]](#).
 - [16] A. J. K. Chua, One-stop function for gravitational-wave detection, identification, and inference, *Phys. Rev. D* **106**, 104051 (2022), [arXiv:2205.08702 \[gr-qc\]](#).

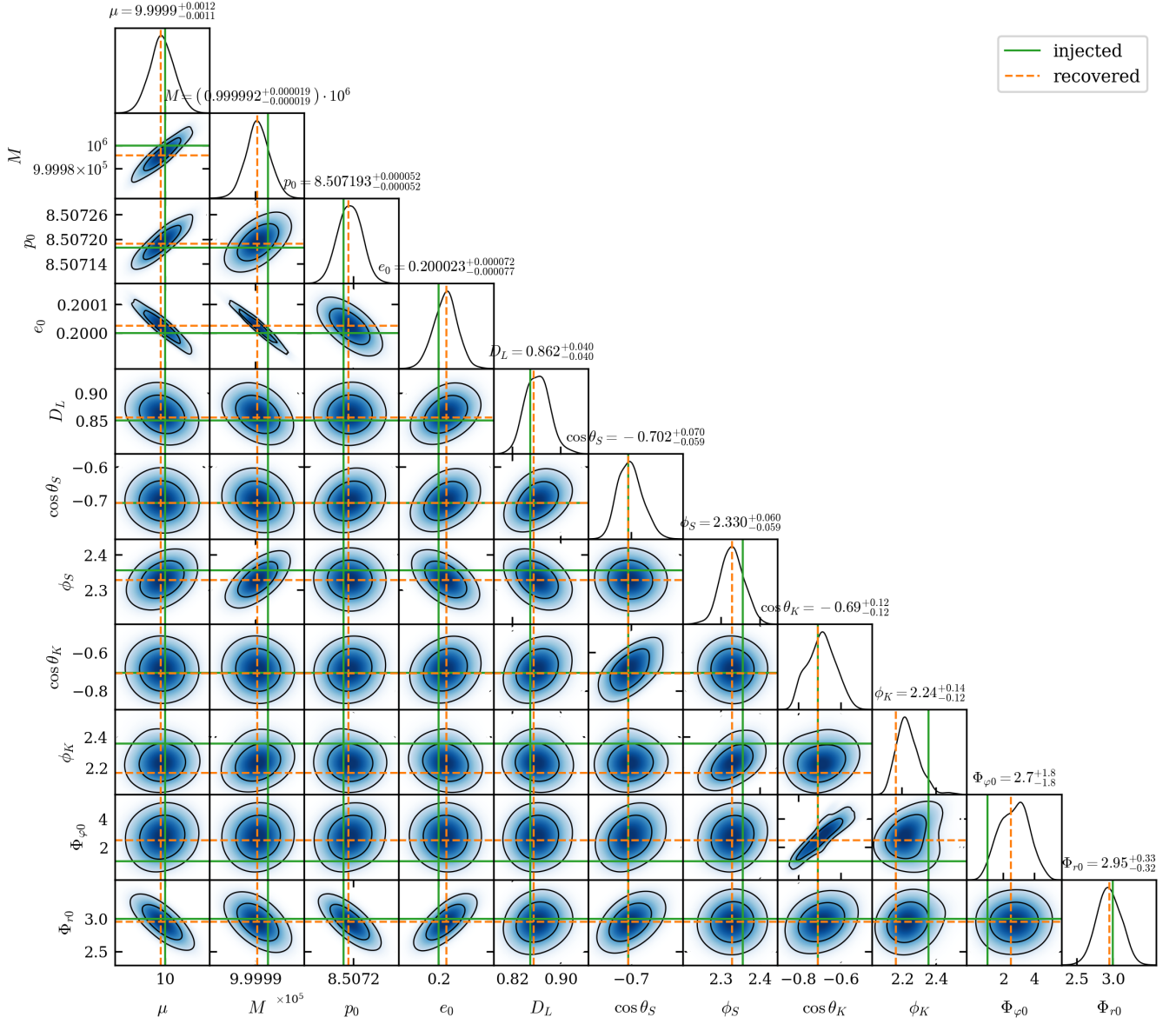


FIG. 11: The green solid lines indicate the injected parameters, while the orange dashed lines represent the recovered parameters, θ_{MLE} , as listed in Table III. The blue contours represent the 68% and 95% confidence regions of the parameter estimation. The posterior distribution is derived using θ_{MLE} as the starting point for the MCMC chain.

- [17] Y. Wang, Y. Shang, S. Babak, Y. Shang, and S. Babak, EMRI data analysis with a phenomenological waveform, *Phys. Rev. D* **86**, 104050 (2012), [arXiv:1207.4956 \[gr-qc\]](#).
- [18] C. Badger, J. A. Font, M. Sakellariadou, and A. Torres-Forné, High-speed reconstruction of long-duration gravitational waves from extreme-mass-ratio inspirals using sparse dictionary learning, *Phys. Rev. D* **110**, 064074 (2024), [arXiv:2407.02908 \[gr-qc\]](#).
- [19] Q. Yun, W.-B. Han, Y.-Y. Guo, H. Wang, and M. Du, The detection, extraction and parameter estimation of extreme-mass-ratio inspirals with deep learning, *Sci. China Phys. Mech. Astron.* **68**, 210413 (2025), [arXiv:2311.18640 \[gr-qc\]](#).
- [20] X.-T. Zhang, C. Messenger, N. Korsakova, M. L. Chan, Y.-M. Hu, and J.-d. Zhang, Detecting gravitational waves from extreme mass ratio inspirals using convolutional neural networks, *Phys. Rev. D* **105**, 123027 (2022), [arXiv:2202.07158 \[astro-ph.HE\]](#).
- [21] C.-Q. Ye, H.-M. Fan, A. Torres-Orjuela, J.-d. Zhang, and Y.-M. Hu, Identification of gravitational waves from extreme-mass-ratio inspirals, *Phys. Rev. D* **109**, 124034 (2024), [arXiv:2310.03520 \[gr-qc\]](#).
- [22] T. A. Prince, M. Tinto, S. L. Larson, and J. W. Armstrong, Lisa optimal sensitivity, *Physical Review D* **66**, 122002 (2002).
- [23] M. Vallisneri, Synthetic lisa: Simulating time delay interferometry in a model lisa, *Physical Review D* **71**, 022001 (2005).

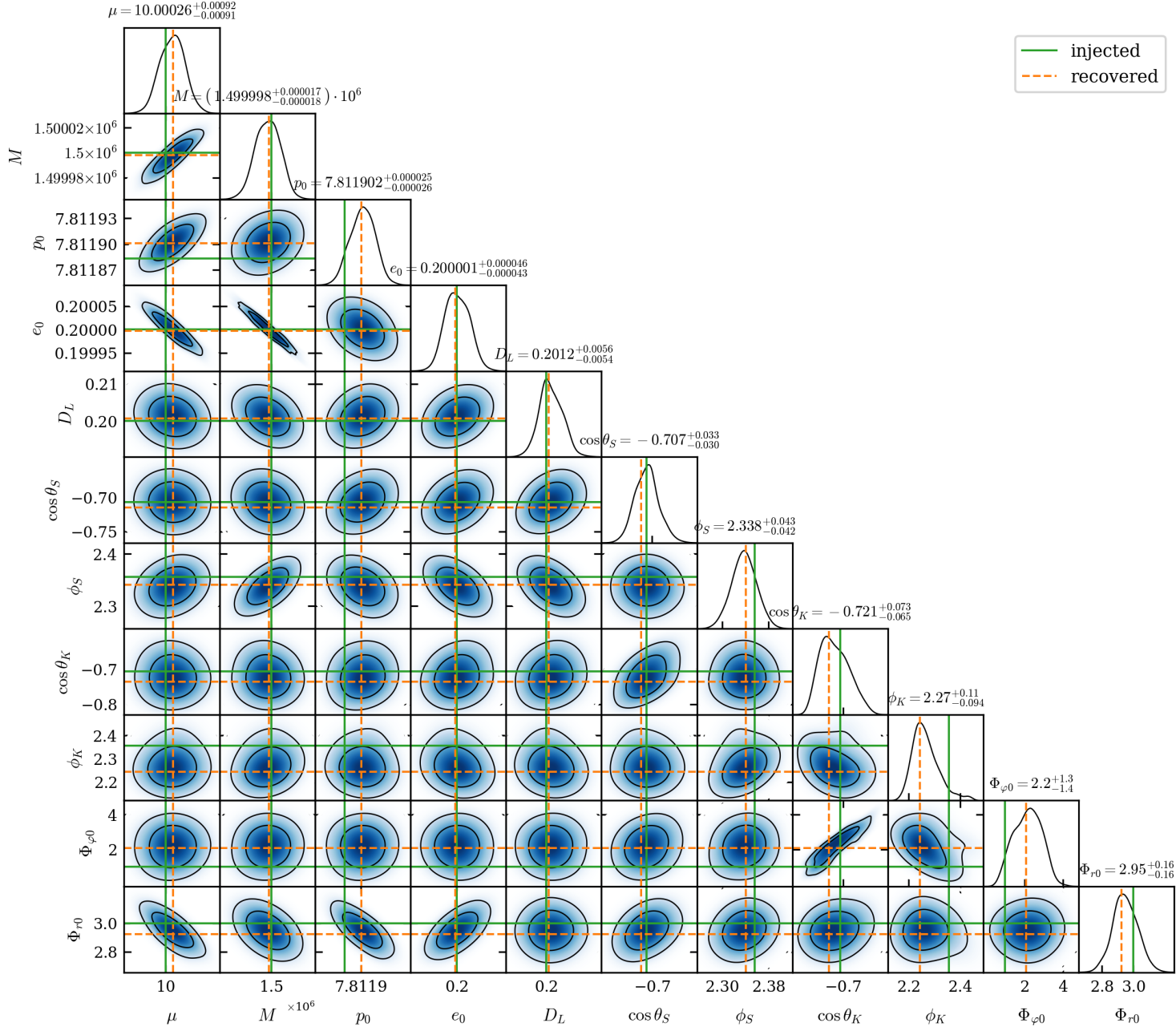


FIG. 12: Corner plot of the increased mass signal. The injected parameters are shown as green solid lines, while the recovered parameters, θ_{MLE} , are indicated by orange dashed lines, where the values of the increased mass signal are presented in Table IV. The blue contours depict the 68% and 95% confidence regions of the parameter estimation.

The posterior distribution is generated using θ_{MLE} as the initial point for the MCMC chain.

- (2005).
- [24] T. B. Littenberg, N. J. Cornish, K. Lackeos, and T. Robson, Global analysis of the gravitational wave signal from galactic binaries, *Phys. Rev. D* **101**, 123021 (2020).
 - [25] A. J. K. Chua, M. L. Katz, N. Warburton, and S. A. Hughes, Rapid generation of fully relativistic extreme-mass-ratio-inspiral waveform templates for LISA data analysis, *Phys. Rev. Lett.* **126**, 051102 (2021), [arXiv:2008.06071 \[gr-qc\]](#).
 - [26] M. L. Katz, L. Speri, A. J. K. Chua, C. E. A. Chapman-Bird, N. Warburton, and S. A. Hughes, [BlackHolePerturbationToolkit/FastEMRIWaveforms: Frequency Domain Waveform Added!](#) (2023).
 - [27] A. J. Chua, C. R. Galley, and M. Vallisneri, Reduced-order modeling with artificial neurons for gravitational-wave inference, *Phys. Rev. Lett.* **122**, 211101 (2019), [arXiv:1811.05491 \[astro-ph.IM\]](#).

- [28] R. Fujita and M. Shibata, Extreme mass ratio inspirals on the equatorial plane in the adiabatic order, *Phys. Rev. D* **102**, 064005 (2020), [arXiv:2008.13554 \[gr-qc\]](#).
- [29] L. C. Stein and N. Warburton, Location of the last stable orbit in Kerr spacetime, *Phys. Rev. D* **101**, 064007 (2020), [arXiv:1912.07609 \[gr-qc\]](#).
- [30] A. J. Chua and J. R. Gair, Improved analytic extreme-mass-ratio inspiral model for scoping out eLISA data analysis, *Class. Quant. Grav.* **32**, 232002 (2015), [arXiv:1510.06245 \[gr-qc\]](#).
- [31] A. J. Chua, C. J. Moore, and J. R. Gair, Augmented kludge waveforms for detecting extreme-mass-ratio inspirals, *Phys. Rev. D* **96**, 044005 (2017), [arXiv:1705.04259 \[gr-qc\]](#).
- [32] L. Barack and C. Cutler, LISA capture sources: Approximate waveforms, signal-to-noise ratios, and parameter estimation accuracy, *Phys. Rev. D* **69**, 082005 (2004), [arXiv:gr-qc/0310125](#).
- [33] L. Speri, M. L. Katz, A. J. Chua, S. A. Hughes, N. Warburton, J. E. Thompson, C. E. Chapman-Bird, and J. R. Gair, Fast and fourier: extreme mass ratio inspiral waveforms in the frequency domain, *Frontiers in Applied Mathematics and Statistics* **9**, 1266739 (2024).
- [34] A. J. Chua, M. L. Katz, N. Warburton, and S. A. Hughes, Data for fast emri waveforms, [10.5281/zenodo.3981654](#) (2020).
- [35] C.-Q. Ye, H.-M. Fan, A. Torres-Orjuela, J.-d. Zhang, and Y.-M. Hu, Identification of gravitational waves from extreme-mass-ratio inspirals, *Physical Review D* **109**, 124034 (2024).
- [36] M. Katz, CChapmanbird, L. Speri, N. Karnesis, and N. Korsakova, [mikekatz04/lisaanalysistools: First main release](#). (2024).
- [37] M. de Carvalho, *Mean, what do you mean?* (2016).
- [38] P. S. Bullen, The power means, in *Handbook of Means and Their Inequalities* (Springer Netherlands, Dordrecht, 2003) pp. 175–265.
- [39] S. H. Strub, L. Ferraioli, C. Schmelzbach, S. C. Stähler, and D. Giardini, Global analysis of lisa data with galactic binaries and massive black hole binaries, *Physical Review D* **110**, 024005 (2024).
- [40] S. H. Strub, L. Ferraioli, C. Schmelzbach, S. C. Stähler, and D. Giardini, Accelerating global parameter estimation of gravitational waves from galactic binaries using a genetic algorithm and gpus, *Physical Review D* **108**, 103018 (2023).
- [41] N. Karnesis, M. L. Katz, N. Korsakova, J. R. Gair, and N. Stergioulas, Eryn: a multipurpose sampler for bayesian inference, *Monthly Notices of the Royal Astronomical Society* **526**, 4814 (2023).
- [42] M. Katz, N. Karnesis, and N. Korsakova, [mikekatz04/eryn: first full release](#) (2023).
- [43] D. Foreman-Mackey, D. W. Hogg, D. Lang, and J. Goodman, emcee: the mcmc hammer, *Publications of the Astronomical Society of the Pacific* **125**, 306 (2013).
- [44] P. Virtanen, R. Gommers, T. E. Oliphant, M. Haberland, T. Reddy, D. Cournapeau, E. Burovski, P. Peterson, W. Weckesser, J. Bright, *et al.*, SciPy 1.0: Fundamental algorithms for scientific computing in Python, *Nature Methods* **17**, 261 (2020).
- [45] R. Storn and K. Price, Differential evolution—a simple and efficient heuristic for global optimization over continuous spaces, *Journal of global optimization* **11**, 341 (1997).